Model validation and prediction of photoacoustic tumor detection with LDV

Laura Mignanelli [*], Marvin Schewe [*], Christian Rembe

Institute of Electrical Information Technology, TU Clausthal, Leibnizstrasse 28, Clausthal-Zellerfeld 38678, Germany

ABSTRACT

Photoacoustic (PA) imaging enables the detection of tumors with ultrasound sensors. A laser Doppler vibrometer (LDV) measures sound waves without contact and may enable non-contact PA imaging (PAI). A successful acquisition with LDV of the PA-signals generated by a tumor irradiated by a pulsed laser depends on several factors: the metrological characteristics of the LDV, the characteristics of the laser pulse as well as the properties of the tumor and of the tissue. In this work, we prove with experiments on tissue-mimicking phantoms the validity of a simulation model based on prior work. We use the validated model to simulate the photoacoustic tumor detection with LDV. Subsequently, we estimate the photoacoustic tumor detection capabilities of a self-designed LDV with the validated model. We derive the limits for the minimal detectable size of tumors for a given depth in tissue. The smallest inclusion detected with our LDV-system on a tissue-mimicking phantom was a sphere with a radius of 200 µm at a depth of 14 mm. With our experimentally validated model, we have predicted the possibility to detect an inclusion in breast tissue with a radius up to approximately 300 µm at a depth of 22 mm.

1. Introduction

Non-contact health monitoring of vital signs has become a potential alternative to classical monitoring methods [1–6]. A non-contact monitoring could be expanded to applications such as ultrasonography [7] and photoacoustic imaging (PAI) or photoacoustic tomography (PAT) [8–10] where acoustic waves are generated in the body and are used for tomographic measurements.

Presently used transducers for medical ultrasound (US) and PAI have some limitations. Their disadvantages result mainly from the contact nature of the technology, such as the need for a coupling medium and the sensitivity to compression, which affects the image quality [11]. Furthermore, US transducers have a finite aperture size, which is disadvantageous for the quality of the reconstructed image since the algorithms for image reconstruction assume a point detector [11,12]. The narrow frequency bandwidth of these sensors of a few hundred kHz at most forbids the detection of differently sized objects and limits the spatial resolution [11]. A full non-contact laser ultrasound (LUS) imaging [13] employs laser light instead of ultrasound probes for both, the generation and the detection of the pulse. In particular, an interferometer with a bandwidth of 2.5 MHz detects the generated wave on the surface. Reference [13] demonstrates the feasibility of a full non-contact ultrasound system for measurements in tissue-mimicking phantoms, animal tissue and humans in vivo. However, biological structures with low acoustic contrast such as early stage tumors in tissue are difficult to detect with US and LUS.

Photoacoustic imaging can overcome these limitations. PAI is an imaging technique based on the PA effect: a short-pulse light source irradiates the tissue and leads to the generation of a broadband PA-wave that propagates through the tissue. The PA-wave is detected with ultrasound transducers and an absorption map of the irradiation is computed. The main applications of PAI are the imaging of molecules, microvasculature, tumors, the brain, and small animals [8–10]. Some structures have low acoustic contrast compared to the surrounding tissue, but relevant differences in optical properties, as for the case of early stage tumors. Therefore, the photoacoustic imaging technique is more promising for the detection of small tumors. In applications where contact with the tissue is not desired or not possible, the commonly used ultrasound contact sensors suffer from limitations. These limitations could be overcome by non-contact photoacoustic imaging for example in peculiar applications like image guided surgery, wound assessment and ophthalmology [11].

In this work, a laser Doppler vibrometer (LDV) is investigated as a non-contact alternative for an US-sensor for PAI because LDV measures broadband signals. Laser Doppler vibrometry is an interferometric technique which is widely used to measure the vibrations in various engineering applications. An LDV is composed of a laser-based interferometer and a broadband decoder. The decoder outputs a broadband displacement or velocity signal in dependence on the demodulation scheme (phase or frequency demodulation). The laser typically has a wavelength of $\lambda = 633$ nm or $\lambda = 1550$ nm [14,15]. The laser beam is split in two beams: a reference and a measuring beam. The reference beam remains inside the measuring head and the measuring beam impinges on the target, the back-scattered light is collected. If the target is moving, the back-scattered light has a shift in frequency due to the Doppler effect, which is related to the velocity/displacement of the vibrations [14,15]. The sensitivity of the LDV is sufficient to detect photoacoustic waves generated by a laser pulse that has an acceptable fluence for human tissue [11,16–18]. Interferometer systems can have different bandwidth depending on the design, the interferometers of the cited Papers are in the range of few (1–3) MHz. Reference [16] discusses non-contact measurements of photoacoustic signals with a commercial laser Doppler vibrometer. The LDV was integrated to a rotational photoacoustic data acquisition system to realize a photoacoustic tomography setup. This system resolves spherical inclusions of 500 μm and multi-layered structures with optical contrast in strongly scattering medium. The LDV discussed in [16] measured the structure of an artificial pig brain with an improved setup. The authors measured the noise equivalent detection limits of their specific specimen and experimental setup, and it results in 810 Pa over 1.2 MHz bandwidth. Other examples of PAI measurements utilizing an LDV are presented in [17,18]. All these examples demonstrate the possibility to detect PA-signals with an LDV. However, a discussion about the general detection limits is missing in the literature. The amplitude and time characteristics of the PA signals are related to the geometry and the optical properties of the investigated object. A successful detection of these signals depends on the metrological characteristics of the detector. In a previous paper [19], we made a preliminary analysis to demonstrate that under certain bandwidth and resolution conditions, PA detection of buried spheres with an LDV is feasible.

A model was introduced that allows the simulation of the propagation and detection of PA signals with an LDV. In this work, we improved and validated the model by performing experiments on silicone tissue-mimicking phantoms that have similar properties as breast tissue. The validated model with breast-tissue parameters reveals the limits of tumor detection with LDV-based PAI for the first time. With the validated model, the estimation of the measuring range in terms of minimal detectable radius and tumor position is possible and reliable. This aspect was not analyzed in the previous studies. In addition, we predict with the validated model the limits of PAI performed with a self-designed LDV for application in breast tissue.

2. Material and methods

2.1. Photoacoustic imaging

Photoacoustic imaging [8–10] is a well-known technique employed for material inspection and, in bioengineering, for hemodynamic monitoring, for detection of brain lesions and for breast cancer diagnosis. The light of a short laser pulse is locally absorbed by the tissue. The temperature of the irradiated object rises and, through thermoelastic expansion, the pressure rises too, and a pressure wave propagates through the tissue. The schematic for a photoacoustic measurement is shown in Fig. 1.

For photoacoustic measurements, a laser with a fluence F_0 excites the tissue with a depth d. Inside the tissue is a sphere with radius R_S at a distance z_S from the irradiated surface, representing a tumor. At the opposite side the measurement beam of the LDV is positioned on the
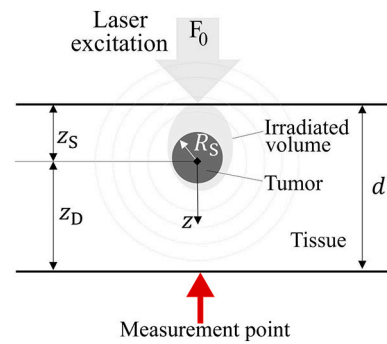

Fig. 1. Schematic of the setup for PA measurements. A laser with the fluence F_0 excites the tissue with a total depth of d. The sphere with the radius R_S is located at a distance z_S from the irradiated surface and represents a tumor. The measurement point of the LDV is positioned on the opposite side of the laser excitation and has a distance of z_D from the center of the tumor (transmission configuration). The detection can also occur from the same side of the excitation (reflection configuration).

measurement point with a distance z_D from the center of the tumor. The propagation of the PA-pressure wave is described in detail in [8,10,20]. In first approximation, an early stage heated tumor in breast tissue could be represented as a homogeneously heated sphere [21]. Tumors have a higher blood content with respect to the surrounding tissue and, therefore, have a higher light absorption at characteristic wavelengths. The pressure wave resulting from the irradiation of a sphere is a bipolar pressure signal with a N-shape [20]. It has a typical duration

$$\tau = \frac{2R_S}{v_s} \tag{1}$$

depending on the radius of the sphere R_S and the sound velocity in medium v_s [20]. The frequency spectrum also depends on the size of the object. Objects with small radius result in more broadband signals with respect to objects with large radius. The frequency spectrum is shown in references [22, 23] with a characteristic central frequency $f_{c,S} = \frac{0.66}{\tau}$. The amplitude of the positive peak in time domain p_M of the N-shaped signal pattern at the measurement point with the distance z_D from the center of the sphere is here approximated as in [19].

$$p_M = \frac{1}{2z_D} p_0 R_S e^{-\bar{\mu}_{att} \cdot z_D} = \frac{1}{2z_D} \Gamma \mu_a F R_S e^{-\bar{\mu}_{att} \cdot z_D}, \tag{2}$$

where p_0 is the initial pressure rise at the time $t = 0$ s in the sphere, which is homogeneously heated, Γ is the Grüneisen parameter, μ_a is the optical absorption coefficient of the sphere at the wavelength of the laser, F is the laser fluence and $\bar{\mu}_{att}$ is a factor for the acoustic attenuation. The value of the fluence F is here assessed as the solution of the diffusion approximation in one dimension [24,25].

$$F = F_0 e^{-\mu_{eff} z_S}, \tag{3}$$

where F_0 is the fluence at the surface after specular reflection losses, μ_{eff} is the effective optical attenuation in the tissue and z_S is the distance from the irradiated surface to the center of the sphere, i.e. penetration depth. For a detailed analysis, F should include an additional term accounting for the increase of fluence under the surface.

The acoustic attenuation of the pressure wave traveling through a medium plays an important role for the correct reconstruction of the photoacoustic image. For algorithms about image reconstruction in PAI, the reader may refer to [9,10].

The aim of this work is to understand under which conditions the LDV can detect PA signals. For this analysis, it is sufficient to estimate the attenuation of the main peak of the N-shaped signal. Usually, complex computations are required for an accurate estimation of the acoustic attenuation. Here, the acoustic attenuation $\bar{\mu}_{att}$ is estimated as

the mean value of the attenuation coefficient between the characteristic frequencies at the half-power bandwidth with the lower frequency $f_{L,-3dB}$ and the upper frequency $f_{H,-3dB}$. Usually, the pressure wave is detected with ultrasound sensors. In the case of contactless measurements with LDV, the pressure wave is detected with the laser at the measurement point. The LDV acquires velocity or displacement signal at the boundary between skin and air, which corresponds to the particle velocity or particle displacement [19]. The velocity is directly proportional to the pressure, therefore the velocity signal presents also the typical N-shape with the positive peak v_M [19,26].

$$v_M = \frac{2p_M}{Z} \tag{4}$$

where Z is the acoustic impedance, i.e. the product between the sound velocity v_s and the density of the medium ρ. The factor 2 results from the fact that the surface displacement is twice as large as the particle displacement inside the medium [26]. The displacement signal is obtained by integrating the velocity signal over time [19] and its maximum s_M is

$$s_M = \frac{p_M \cdot \tau}{2 \cdot Z} = \frac{R_S^2}{Z \cdot v_s} \frac{1}{2z_D} \Gamma \mu_a F e^{-\bar{\mu}_{att} z_D}. \tag{5}$$

To acquire PA signals without degradation, two conditions need to be fulfilled [19].

Condition 1: Bandwidth

For enhanced sensitivity, a relative bandwidth B_{rel} of 1.5 with respect to the central frequency f_c is required [27].

$$B_{rel} = \frac{B}{f_c} = \frac{f_H - f_L}{f_c}. \tag{6}$$

where $B = f_H - f_L$ is the measurement bandwidth of the sensor with the upper frequency f_H and the lower frequency f_L. Assuming a symmetrical bandwidth around the central frequency, the upper and lower frequency can be written as $f_H = f_c\left(1 + \frac{1}{2} \cdot B_{rel}\right)$ and $f_L = f_c\left(1 - \frac{1}{2} \cdot B_{rel}\right)$. Therefore, according to [27] and Eq. 6, this allows the determination of a maximum frequency $f_{c,S,max}$ as a function of the upper frequency of the sensor f_H that allows good detection of the PA signals. The lower frequency $f_L = f_c\left(1 - \frac{1}{2} \cdot B_{rel}\right)$ is inserted into Eq. 6 and is solved for f_c to obtain

$$f_{c,S} = \frac{0.66}{\tau} \leq \frac{f_H}{1 + \frac{1}{2} \cdot B_{rel}} = f_{c,S,max}. \tag{7}$$

For a proper reconstruction of a PA-signal with LDV, the central frequency of the PA-signal, $f_{c,S}$, has to be lower than the maximal central frequency, $f_{c,S,max}$, detectable with the bandwidth of the sensor by considering the detection condition of Eq. 7.

For the specific case of our LDV system, which consists of a self-made IR-LDV and the commercial decoder LDV OFV-2500-2 (Polytec GmbH), the bandwidth is limited by the decoder. For the selected measurement range, this results in $f_L = 0.5$ Hz ≈ 0 Hz and $f_H = 3$ MHz. Eq. 7 thus yields a maximal detectable central frequency $f_{c,S,max} = 1.71$ MHz. The radius of the minimal detectable object $R_{S,min}$ can then be computed by inserting τ from Eq. 1 in Eq. 7 and by setting $f_{c,S} = f_{c,S,max}$

$$R_{S,min} = 0.33 \frac{v_s}{f_{c,S,max}}. \tag{8}$$

Condition 2: Amplitude

The amplitudes p_M, v_M or s_M have to be greater than the resolution of the sensor. For the LDV, this condition can be written as

$$s_{RL}(B) < s_M \tag{9}$$

where $s_{RL}(B) = s_{RL}' \cdot \sqrt{B}$ is the displacement resolution limit of the LDV, B is the bandwidth, s_{RL}' is the displacement resolution at $B = 1$ Hz and s_M according to Eq. 5.

The commercial decoder has a displacement resolution limit at 1 Hz

measured on a mirror of $s_{RL}' = 53$ fm/$\sqrt{\text{Hz}}$. Therefore, its displacement resolution limit is

$$s_{RL}(B) = s_{RL}'\sqrt{B} = 53 \frac{\text{fm}}{\sqrt{\text{Hz}}} \cdot \sqrt{3 \text{ MHz}} = 92 \text{ pm}. \tag{10}$$

To evaluate the limits of LDV for the detection of photoacoustic signals in tissue, the two detection conditions result in a minimally detectable radius $R_{S,min}$ and a noise equivalent displacement amplitude s_{RL}, which the PAI signal amplitude s_M needs to exceed.

2.2. Phantom

Spherical phantoms were produced to mimic tumors and a tissue-mimicking phantom with spherical inclusions was produced to mimic breast tissue with tumors. These phantoms were realized with the two-component silicone Dragon Skin™ 10. The procedure of creating the phantoms consists of mixing the components of the room temperature vulcanizing (RTV) silicone in ratio 1:1. For the production of the spherical phantoms, India ink is added to the mixture to achieve a higher value of optical absorption μ_a with respect to the rest of the phantom. The concentration of India Ink in the total volume was approx. 0.05%. Small air bubbles formed during the stirring were removed with a vacuum pump. The mixture was then poured in the mold and left to harden for seven hours. Fig. 2(a) shows two of the molds for the generation of the spherical phantoms. The two molds of Fig. 2(a) can produce 5 and 4 inclusions with a radius $R_S = 2.5$ mm, respectively. Fig. 2(b) shows a spherical phantom and the tissue-mimicking phantom used to simulate the soft tissue with spherical inclusions inside. The dimensions of the tissue-mimicking phantom are 99.42 mm x 59.67 mm x 33.53 mm, where $d = 59.67$ mm is the width. The phantom has five spherical inclusions S_i where the index $i = 1,2,3,4,5$ identifies the sphere (Fig. 2(b)). The five spheres have a radius $R_S = 2.5$ mm and are positioned at different location defined by the depth z_{S_i} and the distance from the detection surface $z_{D_i} = d - z_{S_i}$, where $z_{S_1} = 2.53$ mm, $z_{S_2} = 3.86$ mm, $z_{S_3} = 4.39$ mm, $z_{S_4} = 5.97$ mm and $z_{S_5} = 6.67$ mm.

Experiments on this tissue-mimicking phantom with inclusions with a radius $R_S = 2.5$ mm were carried out to detect the thermal, acoustic and optic properties of the silicone rubber. We will discuss the determination of these parameters in detail in section 3.1.

An additional tissue mimicking phantom with an inclusion with a radius $R_S = 200$ µm was built (see Fig. 2(c)) and used for the validation of the model. The inclusion is located at a distance of approximately 14 mm from one surface and 2 mm from the other one along the measurement direction.

As we will explain in more detail later, this radius is only slightly above the minimally detectable radius according to Eq. 8. Due to the difficult fabrication process of the smaller sphere, deviations from the already validated model with the larger spheres may occur. For example, the fluence approximation used in the model or the optical properties such as the optical absorption may no longer be valid or may be different. As a result, the measurement results might diverge from the model.

2.3. Setup

Fig. 3(a) shows the scheme and a photo of the setup used for PAI measurements with LDV on silicone rubber phantoms.

The photoacoustic excitation was performed with the pulsed laser Eazy-Brilliant (Quantel). The Eazy-Brilliant is a Q-switch Nd-Yag Laser with a 1064 nm wavelength, a maximal energy of 330 mJ, a pulse duration of 5 ns and a beam diameter of 6 mm.

To adjust the energy of the laser beam, the variable attenuator 2-EWP-T-1064 of the company Altechna was placed at the exit of the laser beam. A beam expander with a magnitude factor of 3 provides a wider spot at the specimen. Thus resulting in a beam diameter of about
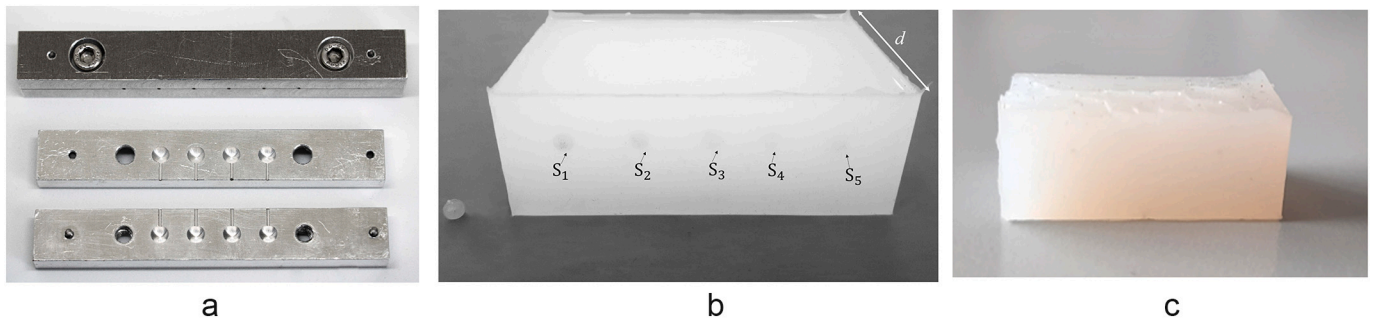
Fig. 2. (a) Examples of the molds for the generation of four silicone rubber spheres with radius $R_S = 2.5$ mm. Top: combined mold. Middle: top mold. Bottom: bottom mold. The top and bottom mold are each a negative for the upper and lower half of the spheres. (b) Spherical phantoms simulating the tumors and phantom with spherical inclusions used for the simulation of breast tissue with tumors. (c) Phantom with a small inclusion with radius $R_S = 200$ μm.
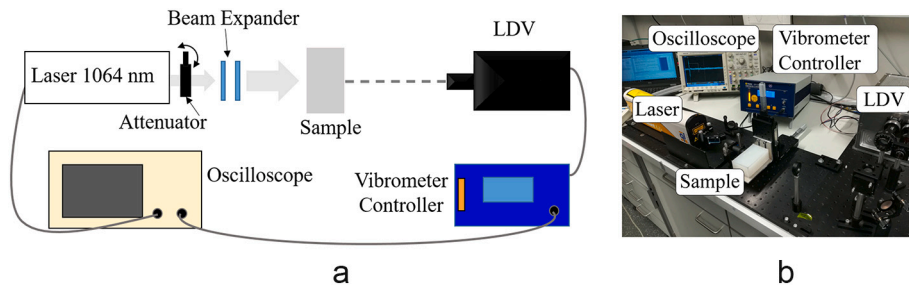

Fig. 3. (a) Schematic and (b) photo of the measurement setup.

18 mm for the experiments. The LDV laser beam impinged on the phantom from the opposite side with respect to the excitation. We used a self-developed infra-red (IR) LDV for all experiments because it is substantially more sensitive compared to our available commercial LDVs with HeNe-lasers [28]. The heterodyne photodetector signal was demodulated by the vibrometer controller (OFV-2500-2 Polytec). The demodulated velocity signal and the Q-switch output of the excitation laser were acquired with an oscilloscope and the data was transferred to a PC. The sampling frequency of the oscilloscope was set to 50 MHz. A measurement consists of a time-average of 128 signals. The displacement resolution of this setup on silicone rubber phantom was measured resulting in $s_{RL,exp} = 64.30$ pm. The displacement resolution was

calculated by determining the noise floor of the vibrometer on silicone with a spectrum analyzer to approx. $0.42\,\text{pm}/\sqrt{\text{Hz}}$ and by multiplying with the square root of the bandwidth of the detector divided by the number of averages $s_{RL,exp} = 0.42\,\text{pm}/\sqrt{\text{Hz}} \cdot \sqrt{3\,\text{MHz}/128}$. The Q-switch signal was employed for the synchronization of the time averaging process and for the identification of the time instant of the laser shot. Measurements were performed on the tissue mimicking phantom of Fig. 2(b) in absence and in presence of the five spherical inclusions. The low-frequency and the high-frequency noise was filtered with a wavelet-denoising filter exploiting the Daubechies wavelet 'db4' [29,30]. The schematic of the setup and the signals of these measurements are shown in Fig. 4. Measurements were also performed on the tissue mimicking
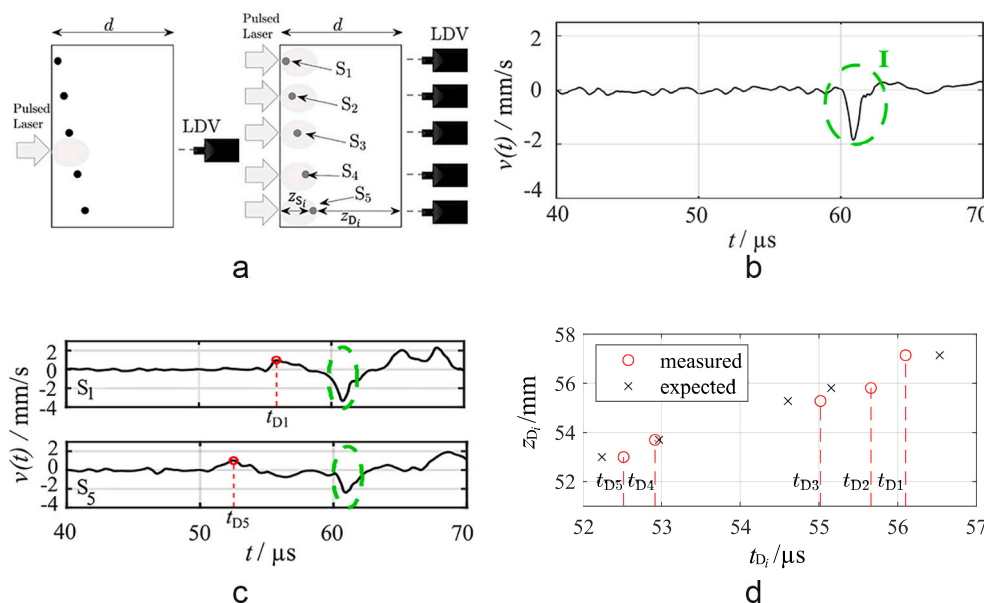

Fig. 4. (a) Schematic of the measurements on the tissue mimicking phantom without (left) and with (right) inclusions underneath. (b) LDV-Velocity signal obtained with the setup on the left in (a). Pattern I (green dashed ellipse) represents the vibrations generated by the irradiated surface. (c) Two velocity signals obtained with the setup on the right in (a). The green dashed ellipses show the same pattern I of (b). (d) The black crosses represent the expected time points and the red circles the measured time points t_{D_i}, at which the maximum of the N-shaped signal is generated by the sphere with radius $R_S = 2.5$ mm and obtained with the setup on the right in (a). Two examples are shown in (c). (For interpretation of the references to colour in this figure legend, the reader is referred to the web version of this article.)

phantom of Fig. 2(c) in absence and in presence of the small inclusions with two different configurations (front and reverse). In the front configuration, the penetration depth of the phantom was $z_S \approx 14$ mm and the distance from the detection surface $z_D \approx 2$ mm. In the reverse configuration, the phantom was positioned the other way around; hence the penetration depth was $z_S \approx 2$ mm and the distance from the detection surface $z_D \approx 14$ mm.

3. Results

3.1. Identification

The signals acquired with the LDV are presented in this section. Fig. 4 (a) shows the setup for measurements on the tissue mimicking phantom shown in Fig. 2(b) with the spheres with a radius of $R_S = 2.5$ mm. Fig. 4 (b) presents the LDV signal acquired with the left configuration of Fig. 4 (a), i.e. when the excitation laser impinges on the part of the phantom without inclusions underneath.

The signals were filtered with the wavelet-denoising filter mentioned in Section 2.3. In particular, the difference between the approximation at level 5 and at level 11 of the wavelet decomposition 'db4' [29] were subtracted, resulting in a band-pass filter between the frequencies $f = 12.21$ kHz and $f = 781.25$ kHz. Fig. 4(b) shows the velocity signal which has a characteristic pattern. This pattern I represents the vibrations generated by the irradiated surface. Its amplitude and time characteristics are related to optical, thermal and acoustic properties of the irradiated material, the characteristics of the laser irradiation and the boundary conditions [31,32]. The signal of the irradiated surface of the tissue-mimicking phantom presents a stress (i.e. velocity) transient with a negative peak. Pattern I occurs at a time equal to the distance $d = 59.67$ mm that the wave travels divided by the sound velocity. The descending peak starts at the time $t \approx 60$ µs after the laser shot ($t = 0$ s) and the negative peak appears at $t \approx 61$ µs. The LDV-measurements on the tissue mimicking phantom of Fig. 2(b) in presence of the inclusions were acquired at each inclusion position for different fluence values F_0 (≈ 715 J/m^2, ≈ 1365 J/m^2, ≈ 1912 J/m^2, ≈ 2160 J/m^2). The measurement were performed with the right setup of Fig. 4(a). The characteristic pattern is recognizable for all measurements and fluence values. As an example, we show in Fig. 4(c) the LDV signals in correspondence of the sphere 1 and 5 with the fluence value $F_0 \approx 1912$ J/m^2. The obtained signals show both patterns generated by the sphere and by the irradiated surface. The two exemplary signals of Fig. 4(c) present the pattern I. In particular, the negative peak (green dashed ellipse) occurs at the time $t \approx 61$ µs as in Fig. 4(b). The N-shaped pattern generated by the spheres is also present in all the signals; its positive peak is identified with a red circle (Fig. 4(c)). The sphere S_1 generates the velocity signal denoted with S_1; the same applies to the other spheres S_i. The sphere S_1 is positioned at the smallest depth $z_{S_1} = 2.53$ mm and, therefore, at the greatest distance $z_D = z_{D1}$ from the measurement point. The sphere S_5 is positioned at the greatest depth $z_S = z_{S_5}$ and the smallest $z_D = z_{D5}$ and is therefore closest to the measurement point. The time points t_{D_i} of the positive peak for all signals generated for different z_{D_i} are shown as a red circle in Fig. 4(d). As expected, with increasing depths z_D the positive peaks of the N-shaped signal is visible at a later time in the signal. The expected time points as a function of distance and sound velocity are also shown as black crosses. The difference between the expected and the measured values can be explained due to the amplitudes not being determined accurately enough from the time signals. Furthermore, measurement deviations of z_D of 1 mm already lead to deviations of more than 1 µs. Note that the delay of the N-shaped signal depends on the distance between the surface of the acquisition and the absorbing sphere z_{D_i}. For the sphere S_1, the negative peak generated by the surface (green dashed ellipse) is not well discernible from the negative peak of the N-shaped signal because of the close distance between the sphere and the surface. Since the other spheres are located at greater depth z_S, the two negative peaks appear separated. The time duration τ of the N-

shaped signals is in the expected range $\tau \approx 4 - 5$ ms for all the five signals.

For the validation of the model, the properties of the silicone rubber must be known. Some of these properties were experimentally determined: the sound velocity $v_{s,sil} = 966$ m/s, the impedance $Z_{sil} = 1.07$ MRayl, the Grüneisen parameter $\Gamma_{sil} = 0.49$ and the acoustic attenuation $\overline{\mu}_{att} = 0.051$ Np/cm. The optical absorption $\mu_{a,sil}$ and the effective optical attenuation $\mu_{eff,sil}$ are unknown parameters and must be determined. Therefore, we conducted measurements on the tissue mimicking phantom shown in Fig. 2(b) with spherical inclusions and its measurement setup shown in Fig. 4 to perform a parameter identification. The parameter identification was performed according to the routine presented in [33] which uses a least-square algorithm. The values of the optical absorption $\mu_{a,sil}$ and of the effective optical attenuation $\mu_{eff,sil}$ obtained are the ones that minimize the cost function g

$$g\left(\mu_{a,sil}, \mu_{eff,sil}\right) = \frac{1}{2}\sum_{i=1}^{N}\left(v_{Mi}\left(\mu_{a,sil}, \mu_{eff,sil}\right) - v_{M,expi}\right)^2, \tag{11}$$

where N represents the number of experiments ($N = 4$ value of fluence F_0 x 5 spheres $S_i = 20$). The function $g(\mu_{a,sil}, \mu_{eff,sil})$ is the square of the norm of the residuum between the simulated data of the peak of the velocity v_M computed with Eq. 4 and the peak $v_{M,exp}$ of the experimental velocity data obtained with the setup of Fig. 4(a) (right) for the four different energy levels of the pulsed laser. According to [33], the quality of the identification is determined with the coefficient of determination R^2

$$R^2 = 1 - \frac{\sum_{i=1}^{N}\left(v_{M,expi} - v_{Mi}\right)^2}{\sum_{i=1}^{N}\left(v_{M,expi} - \overline{v}_{M,exp}\right)^2}, \tag{12}$$

where $\overline{v}_{M,exp}$ is the mean value of all the experimental data. The value of R^2 varies in the interval $0 \leq R^2 \leq 1$. For a very good fit R^2 has to be $R^2 \approx 1$. The function $g(\mu_{a,sil}, \mu_{eff,sil})$ finds its minimum for $\mu_{a,sil} = 0.3865$ cm^{-1} and $\mu_{eff,sil} = 0.4597$ cm^{-1}. In our experiments, it resulted in $R^2 = 0.9539$; therefore, the quality of the parameter identification is good.

In Table 1, literature values for the optical absorption of an actual tumor $\mu_{a,tum}$ as well as the effective optical attenuation for real tissue $\mu_{eff,tis}$ are shown in addition to the values determined from the parameter identification for our silicone phantom.

With the two parameters identified, all variables from Eq. 5 to determine the displacement as a function of z_S and z_D are known.

The parameters of our silicone phantom differ from the expected parameters of tissue and tumor. While the optical absorption has similar values, the values for the effective optical attenuation are different, because no additional scattering particle were added to the silicone phantom. The introduction of scattering particles would have complicated the model, in particular Eq.3, therefore they were neglected for our initial considerations to minimize the number of unknown variables for the model. Nevertheless, our silicone phantom is suitable for validating the introduced model, since the fundamental requirement of a higher absorption of our phantom in comparison to the surrounding material is satisfied. With a successful model validation of our silicone phantom, we can subsequently apply the real parameters of a tumor and tissue to make predictions for the measurement on real tissue.

Table 1
Determined values for the optical absorption and the effective optical attenuation for our silicon phantom as well as corresponding typical values for real tissue and tumor tissue.

	Optical absorption	Effective optical attenuation
Tissue/Tumor	$\mu_{a,tum} = 0.6$ cm^{-1}	$\mu_{eff,tis} = 1.2$ cm^{-1}
Phantom	$\mu_{a,sil} = 0.3865$ cm^{-1}	$\mu_{eff,sil} = 0.4597$ cm^{-1}

3.2. Validation

To validate the model, further measurements were performed to verify the derived parameters. To additionally test the limits of our LDV system, spheres with a just detectable radius were created. For this purpose, the amplitude of the velocity peak $v_{M,exp}$ of these experiments on the smaller spheres needs to match the value obtained by computing Eq. 4. The radius of the minimal detectable sphere in silicone rubber $R_{S,min,sil}$ can then be calculated according to Eq. 8. The minimal detectable radius resulted in $R_{S,min, sil} = 192$ μm by considering a relative bandwidth $B_{rel} = 1.5$, the maximal frequency of the LDV-bandwidth $f_H = 3$ MHz and the sound velocity of the silicone rubber used $v_s = v_{s,sil} = 996$ m/s. The phantom of Fig. 2(c), which is used for the additional measurements, therefore has inclusions with a radius $R_S \approx 200$ μm, just above the limit of 192 μm.

Depending on the distances from the center of the sphere of the measurement point on the surface z_D and the depth of the sphere in tissue z_S, it is possible to determine for a given fluence F_0 if the sphere is detectable. According to the model of the theory presented in Section 2.1, the detection range for a sphere with a radius R_S can be estimated by verifying the condition of Eq. 9. The maximum of the displacement signal $s_{M,exp}$ calculated with Eq. 5 should be greater than the displacement resolution of the IR-LDV in the experiments $s_{RL,exp}$ as defined in Eq. 9

$$s_{RL,exp} < s_{M,exp} = \frac{R_S^2}{Z_{sil} \cdot v_{s,sil}} \frac{1}{2z_D} \Gamma_{sil} \mu_{a,sil} F_0 e^{-\mu_{eff,sil} z_S} e^{-\bar{\mu}_{att} z_D}, \quad (13)$$

We can then estimate the detection range of a sphere with a radius $R_{S,min, sil} = 192$ μm according to Eq. 13 for silicone rubber phantoms. The resolution of the IR-LDV for the experiments is $s_{RL,exp} = 64.30$ pm. The value of fluence at the surface $F_0 \approx 715$ J/m^2 used in the experiments is chosen for the estimation of the detection range. Fig. 5 shows the calculated detection range for a sphere with the minimal detectable radius for silicone rubber $R_{S,min,sil} = 192$ μm computed according to Eq. 13. The white area identifies where the sphere is detectable and the black area where a detection is not possible i.e. $s_{RL,exp} > s_{M,exp}$. The detectable area is delimited by the penetration depth $z_S \approx 64$ mm and the maximal distance from the measurement point $z_D \approx 3.6$ mm. To confirm the prediction of the detection range, measurements in the detectable and non-detectable range were carried out. It should be noted that the measurements were obtained with a sphere of a radius of $R_S \approx 200$ μm and are therefore only slightly above the minimum detectable radius of 192 μm. The following results should thus be considered in this context. As the model was identified with spheres with a much larger radius, we can expect some deviations. Since the measurement is performed at the absolute detection limit, additional discrepancies due to noise are expected. The aim of our experiments is to validate our
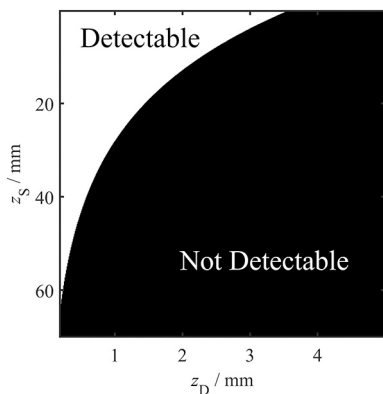

Fig. 5. Detection range of the silicone rubber spheres with radius for a displacement resolution of the experiments $s_{RL,meas} = 64.30$ pm and the fluence $F_0 = 715$ J/m^2.

simplified model for an approximate assessment of the applicability of non-contact PAI measurements. For further research, a more detailed model should be developed that considers additional parameters. For this purpose, an intensive sensitivity analysis of the individual parameters should be performed. At this stage, we have skipped it on purpose, as it is not the focus of the presented work.

First, a measurement was obtained with an inclusion in the detectable range with the penetration depth of the phantom $z_S \approx 14$ mm and the distance from the measurement point $z_D \approx 2$ mm. For a first assessment, an additional measurement with a higher fluence was taken. The fluence was set to $F_0 = 715$ J/m^2 and to $F_0 = 1365$ J/m^2. The two signals in presence of the inclusion are shown in Fig. 6(a) (red line and blue dashed line, respectively). Subsequently, a signal without inclusion was acquired with the fluence $F_0 = 715$ J/m^2 and is presented as a black line in Fig. 6(b) in addition to the signal with the inclusion. All the patterns show a negative peak after 16 μs that corresponds to the acoustic wave generated by the irradiation of the surface (similar to pattern I as shown in Fig. 4(b)). The signal acquired with the inclusion and the fluence $F_0 = 1365$ J/m^2 presents a significantly N-shaped signal at about 2.5 μs, which corresponds to the signal generated by the absorbing sphere with radius $R_S = 200$ μm. The same pattern with a smaller amplitude is identifiable also in the measurement with the inclusion and the fluence $F_0 = 715$ J/m^2. As expected, differences in presence and in absence of the inclusion are noticeable at about 2.5 μs where the characteristic N-shaped signal is identifiable. The real amplitude of the positive peak $v_{M,exp}$ is difficult to calculate since the starting point of the wave is hard to identify due to the existing noise. Therefore, the amplitude is here determined as the difference between the negative and positive peaks of the N-shaped signal divided by two. The expected amplitude for the experiments is $v_M = 6.6 \cdot 10^{-4}$ m/s for the fluence $F_0 = 715$ J/m^2 and $v_M = 1.3 \cdot 10^{-3}$ m/s for the fluence $F_0 = 1365$ J/m^2. The amplitude in the experiments is $v_{M,exp} \approx 2.3 \cdot 10^{-3}$ m/s for the fluence $F_0 = 715$ J/m^2 and $v_{M,exp} \approx 4.0 \cdot 10^{-3}$ m/s for the fluence $F_0 = 1365$ J/m^2. As expected, there is a deviation between the experimental results and the model, due to the difficult fabrication process of the absorbing sphere with a smaller radius used in this experiment. For these specific measurements there is a factor of 3.5 and 3.1 for the velocity amplitude. Several other measurements showed that this factor is in the range of 2.8 to 3.6. The discrepancy in this case seems to be high, but it has to be considered that these measurements were taken at the detection limit and, thus, at a strong noise level. At the detection limit, multiple small influences can already explain the discrepancy between the model and the experiments. The difficulties in making small absorbing spheres with a reproducible amount of ink at the detection limit make it particularly difficult to estimate the fluence correctly. Therefore, we are very much satisfied with the result. We mathematically determined the minimally detectable radius for our model and subsequently had to build a physical phantom to test the model. It is difficult to produce such small silicone spheres (with a radius of 192 μm) accurately. Therefore, we approximated the value to 200 μm for the experiments.

This can cause deviations from the real parameters (e.g. $\mu_{eff,sil}$ and $\mu_{a,sil}$) of the small spheres compared to the parameters determined from the measurements with the large spheres. Eq. 4 shows the influence of these parameters on the calculated amplitude and thus explains deviations between the amplitudes from the experiment and the expected amplitudes from the model.

As mentioned earlier, the measurements were also taken in the just detectable range. Therefore, the absolute deviations with regard to the uncertainty of a measurement at the detection limit and any deviations of the actual parameters of the smaller phantom to the model parameters determined from the larger phantom are in an acceptable range.

For a measurement in the non-detectable range, the phantom was positioned the other way around; hence the penetration depth was $z_S \approx 2$ mm and the distance from the measurement point $z_D \approx 14$ mm.

In the series of measurements with this configuration, the inclusion

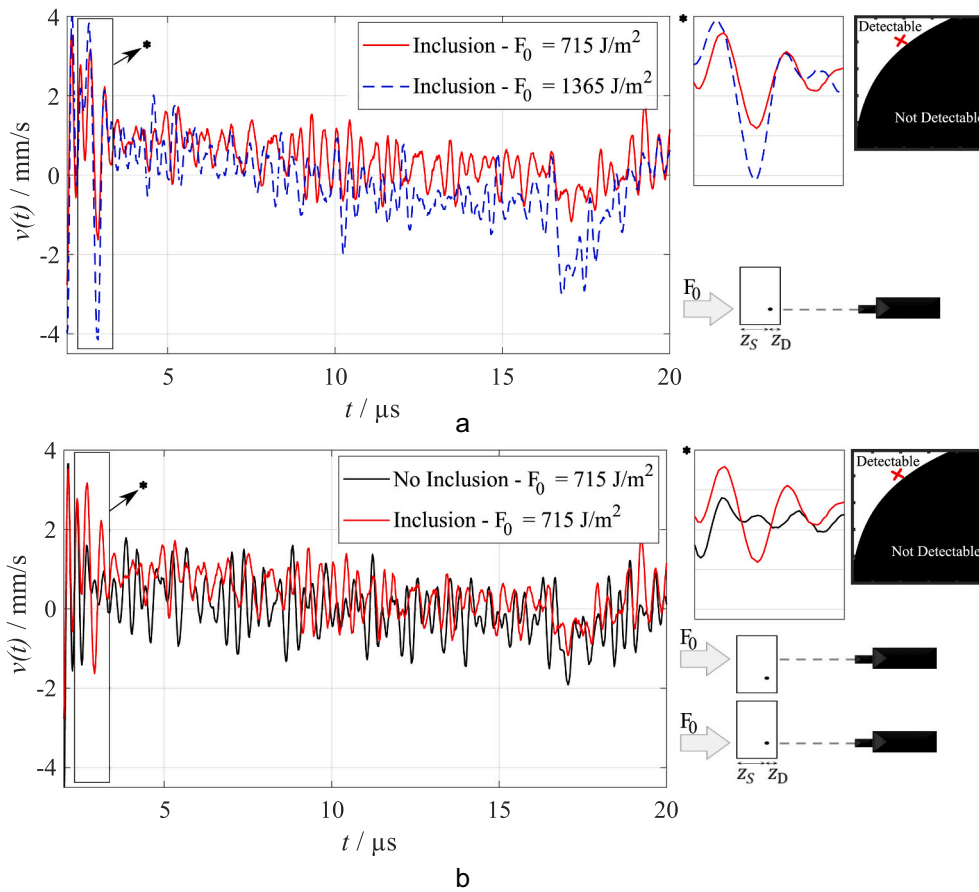**Fig. 6.** Acquired signals in the detectable range ($z_S \approx 14$ mm and $z_D \approx 2$ mm) with and without a small inclusion with radius $R_S \approx 200$ μm. (a) Signals with inclusion and different fluences. (b) Signals with and without inclusion with the same fluence.

should present the N-shaped signal in the velocity signal at about 14 μs, assuming an amplitude above the resolution limit. However, as shown in the magnified plot at the expected time in Fig. 7 there is no significant difference between the measurements with inclusion (red line) and the measurements without it (black line). Even in these measurements, the negative peak at about 16 μs generated by the surface is noticeable.

The measurement performed with the configuration shown in Fig. 6 prove the calculated detection limits that are displayed in Fig. 5 for a fluence value of $F_0 = 715$ J/m². Therefore, the prevision of detection range of the model is correct. In the reverse configuration shown in Fig. 7 the defect was positioned in the non-detectable range. According to the prevision, with the fluence value $F_0 = 715$ J/m², the N-shaped

signal should not be detectable and, as expected, we could not detect it.

4. Discussion

The model presented in Section 2.1 was validated with the experiments on silicone phantoms of Section 3.

So far we have validated our simplified and one-dimensional model on silicone probes. In this section we use breast tissue parameters for the simulation model to estimate the limits in in-vivo experiments in both transmission and reflection configuration. Usually we can expect, that excitation and sensing are performed with one medical scanner from one side (reflection configuration). According to Eq. 8, the radius of the
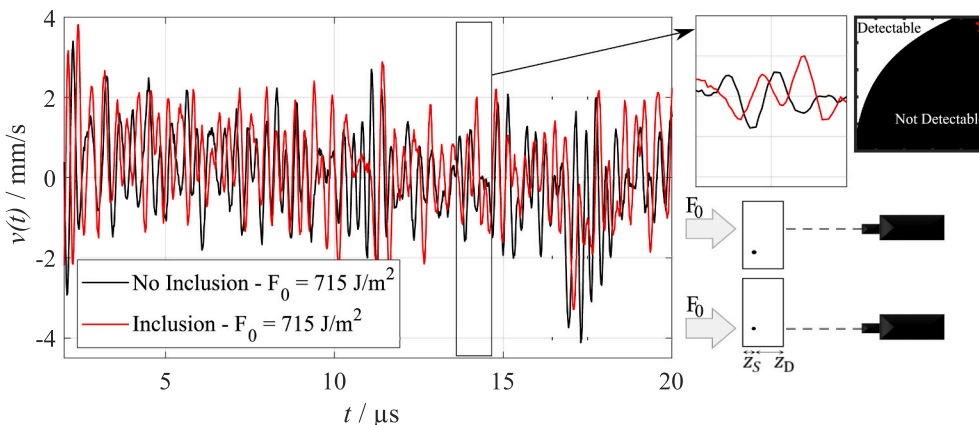

Fig. 7. Acquired signals in the non-detectable range ($z_D \approx 14$ mm and $z_S \approx 2$ mm) with and without a small inclusion with radius $R_S \approx 200$ μm.

minimal detectable object with our setup in breast tissue $R_{S,min}$ results in $R_{S,min} \approx 291$ μm by considering the sound velocity $v_s = 1510$ m/s [34] and a relative bandwidth $B_{rel} = 1.5$ (see Eq. 8). A bandwidth $B_{rel} = 0.75$ provides a good compromise between resolution and noise level [23] leading to a smaller minimal detectable radius $R_{S,min}$. Objects with a radius $R_{S,min}$ are detectable only if the condition of Eq. 9 is met. For the determination of this condition, the maximal amplitude of the photo-acoustic displacement signal generated by an irradiated sphere with the minimal detectable radius s_M is computed and a comparison to the resolution limit of the LDV $s_{RL}(B)$ is carried out according to Eq. 9.

The value of the maximal displacement amplitude s_M for a sphere with radius $R_{S,min}$ can then be evaluated in dependence of the depth of the sphere z_S and distance between the sphere and the sensor z_D. The value of the breast tissue parameters used to compute s_M are the sound velocity $v_s = 1510$ m/s, the impedance $Z = 1.54$ MRayl and the acoustic attenuation $\alpha_0 = 0.75$ dBcm^{-1}MHz^{-1} [34]. The effective optical attenuation depth at the wavelength of the pulsed laser $\lambda = 1064$ nm is $\mu_{eff} = 1.2$ cm^{-1} [23]. The absorption coefficient for normal breast tissue varies in the range $0.03 - 0.05$ cm^{-1} for a wavelength of $\lambda = 1064$ nm [35]; the optical absorption of a tumor is greater. The absorption coefficient $\mu_a = 0.6$ cm^{-1} is employed for the simulation as in [23]. The value of the Grüneisen parameter Γ varies in the range $0.2 - 0.5$ for breast tissue at $37\,^\circ$C [27, p. 423], therefore the mean value $\Gamma = 0.35$ is employed. The maximal allowed fluence for application in human body at $\lambda = 1064$ nm $F_0 = 1000$ J/m^2 is used [36].

Our self-developed LDV provides a signal that has a resolution on a

mirror of approximately 6 fm/$\sqrt{\text{Hz}}$ for an ideal decoder. The commercial velocity decoder used in the experiments is the LDV OFV-2500-2 (Polytec GmbH). The decoder has a resolution of 53 fm/$\sqrt{\text{Hz}}$ and therefore limits the resolution. The resolution of our system for a single measurement, i.e. without averaging the measurements is $s_{RL}(B) = s_{RL}(3\text{MHz}) = 92$ pm. However, such a good resolution is difficult to achieve on bare skin. Skin scattering can be improved with zinc-oxide based cream or with white eye-shadow. Here, we assume optimal conditions of the skin scattering for one single measurement without averaging. Fig. 8(a) shows in white the detection range of the sphere with radius $R_{S,min}$ in function of its depth in tissue z_S and its distance to the measurement point z_D. The white area represents where Eq. 9 is satisfied, i.e. the amplitude s_M is greater than the resolution limit of the LDV-system used in our setup. The black range of Fig. 8(a) identifies where the vibrations of the object are not detectable. The white range is delimited by the penetration depth $z_S \approx 22$ mm if the measurement point is at the distance $z_D = R_{S,min}$. If the penetration depth z_S is equal to $R_{S,min}$, the maximal detection distance z_D is ≈ 3.8 mm.

This can be considered the resolution limit for our LDV-system for a single measurement in breast tissue.

Generally, our model can be used to make different predictions for breast or soft tissue. For example, Fig. 8(b) shows the detection range for a tumor in breast tissue with a radius $R_S = 2.5$ mm, the absorption coefficient $\mu_a = 0.3865$ cm^{-1}, the Grüneisen parameter $\Gamma = 0.49$. Moreover, the fluence $F_0 \approx 715$ J/m^2 and the resolution of our measurements $s_{RL}(B) = s_{RL,exp} = 64.30$ pm obtained by averaging are employed for the
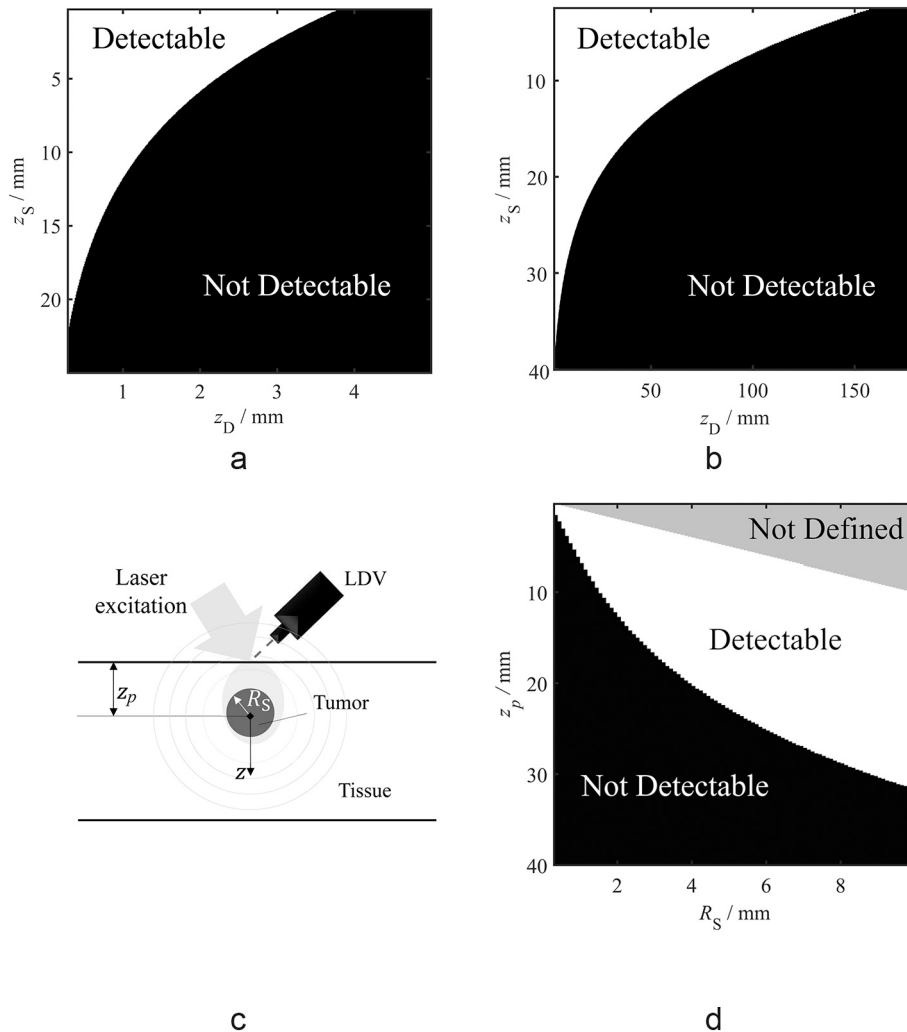
a

b

c

d

Fig. 8. (a) Detection range of our LDV-system in breast tissue for a spherical object with radius $R_{S,min}$ = 291 μm and absorption coefficient $\mu_a = 0.6$ cm^{-1} in breast tissue with the Grüneisen parameter $\Gamma = 0.35$, the fluence $F_0 = 1000$ J/m^2 and detected with the LDV theoretical resolution $s_{RL}(B) = 92$ pm. (b) Detection range of a tumor with a radius $R_S = 2.5$ mm, absorption coefficient $\mu_a = 0.3865$ cm^{-1} in tissue with the Grüneisen parameter $\Gamma = 0.49$, the fluence $F_0 = 715$ J/m^2 and detected with the LDV resolution $s_{RL,exp} = 64.30$ pm obtained by averaging. (c) Setup in reflection configuration with the penetration depth $z_p = z_D = z_S$. (d) Detection range of a tumor in function of its radius R_S and its penetration depth in tissue z_p for the case of measurements in reflection configuration. The plot is obtained with the absorption coefficient $\mu_a = 0.3865$ cm^{-1}, the Grüneisen parameter $\Gamma = 0.49$, the fluence $F_0 = 715$ J/m^2 and the LDV resolution $s_{RL,exp} = 64.30$ pm. The gray region is not defined since $z_p < R_S$.

simulation. The other parameters are the same as the computation of Fig. 8(a). It must be noted that to have a $s_{RL}(B) = s_{RL,exp} = 64.30$ pm in breast tissue, the surface should be treated and the excitation condition should be adapted according to the laser safety norm [36]. In this case, the detection range (white area) is delimited by the penetration depth $z_S = 39.35$ mm and the distance from the measurement point $z_D = 15.85$ cm.

The validated model can be used to make predictions about the detection of tumors for other cases such as measurements in reflection configuration, as shown in Fig. 8(c). In reflection configuration, the excitation and the detection are performed from the same side and, therefore, the tumor is positioned at the same distance z_p from both excitation and detection point. The distance z_p is the penetration depth. Fig. 8(d) shows the detection range of tumors with different radii R_S and optical absorption $\mu_a = 0.3865$ cm^{-1} in breast tissue as a function of the penetration depth z_p according to the setup of Fig. 8(c). The Grüneisen parameter $\Gamma = 0.49$, the fluence $F_0 = 715$ J/m^2 and the LDV resolution $s_{RL,exp} = 64.30$ pm are chosen for the simulation. The other parameters of the simulation are the same as used in Fig. 8(a) and (b). The gray area represents where the simulation has no physical and geometrical meaning ($z_p < R_S$). The white area represents the penetration depths at which the tumor with a radius R_S is detectable; the black range is the range where the tumors are not detectable. From Fig. 8(c) the detection limits of a setup in reflection configuration for measurements in breast tissue can be determined. For example, tumors with a radius $R_S = 4$ mm can be detected up to a penetration depth of $z_p \approx 20$ mm in breast tissue.

The performances of LDV can be improved if the detection bandwidth could be adapted to the dimension of the radius of the searched object, as already shown in [19].

In fact, for radii greater than $R_{S,min}$, the necessary detection bandwidth for a reliable detection of the sphere is narrower (Eq. 7) and the narrower the bandwidth, the lower is the noise level and the lower is the minimal detectable displacement.

Since our LDV-system is currently limited by the resolution of the decoder, the resolution can be improved by using a better decoder with lower noise or by performing our own demodulation of the LDV signal. Thus, the theoretically possible bit resolution of our self developed LDV of approximately $s'_{RL} = 6$ fm$/\sqrt{Hz}$ could be achieved. The theoretical resolution limit for our IR-LDV $s'_{RL,IR} = 6$ fm$/\sqrt{Hz}$ is obtained by considering a decoder with an effective number of bits of 11 Bit, a sampling rate of 250 MS/s and a mirror as the target. The resolution limit of signals measured directly on the skin is higher than 6 fm$/\sqrt{Hz}$, but it can be enhanced by applying zinc-oxide cream or white eye shadow to the measurement point. The use of retro-reflective tape would also increase the displacement resolution limit significantly, but it may obstruct the laser excitation and the contact-less aspect of the technique is somewhat lost.

Another possibility to enhance the measurement on the bare skin, is to increase the laser power of the IR-laser of the LDV, or to perform averaged measurements; in those cases, the laser safety norm must be taken into account [36].

5. Conclusions and outlook

In this work, experiments on tissue-mimicking phantoms prove the capability of LDV for PAI measurements. PAI measurements on a silicon rubber phantom with spherical inclusions were performed with a self-made IR-LDV. The silicone phantom with spherical inclusions mimics the breast or soft tissue with tumors. The acquired signals were used to identify unknown parameters and to validate our model for the generation and propagation of PA signals and its detection with an LDV. We used the validated model to make predictions for measurements in breast tissue in transmission or reflection configuration. Therefore, we can state under which conditions PA measurements and, consequently, PAI with an LDV is feasible. In this context, the bandwidth of the sensor

determines the minimum detectable radius of an object. The analysis shows, for example, that our LDV-system is capable to detect tumors in breast tissue with a radius up to approximately 300 μm located at depth of ≈ 2 cm, if the excitation laser has a wavelength of 1064 nm and a pulse energy of 1000 J/m^2 for a single measurement. Future works are aimed to carry out PAI measurements on optimized tissue phantoms with a multipoint laser Doppler vibrometer [37]. The optimized phantoms should enable more accurate replication of the optical and acoustic properties of real tissue. The multipoint vibrometer allows the simultaneous detection of vibrations at several points, which is advantageous in terms of acquisition time: with one measurement, the vibration of the entire measurement object can be detected and an image can be reconstructed. The multi-point vibrometer also allows three-dimensional measurements, which, in conjunction with suitable algorithms, may allow better localization of the inclusion/tumor.

Data availability

Data underlying the results presented in this paper are not publicly available at this time but may be obtained from the authors upon reasonable request.

Funding

Declaration of Competing Interest

The authors declare that they have no known competing financial interests or personal relationships that could have appeared to influence the work reported in this paper.

Data availability

Data will be made available on request.

References

[1] A. Luik, L. Mignanelli, K. Kroschel, C. Schmitt, C. Rembe, L. Scalise, Laser doppler vibrometry as a noncontact method to detect various degrees of atrioventricular block: a feasibility study, Futur. Cardiol. 12 (2016) 269–279.

[2] L. Scalise, Non contact heart monitoring, in: R.M. Millis (Ed.), Advances in Electrocardiograms, 2012. IntechOpen, Rijeka. (chap. 4).

[3] L. Mignanelli, C. Rembe, Non-contact Health Monitoring with LDV, Springer International Publishing, 2020, pp. 1–8.

[4] H.T. Yen, M. Kurosawa, T. Kirimoto, Y. Hakozaki, T. Matsui, G. Sun, A medical radar system for non-contact vital sign monitoring and clinical performance evaluation in hospitalized older patients, Biomed. Signal Process. Control 75 (2022), 103597.

[5] L. Scalise, U. Morbiducci, Non-contact cardiac monitoring from carotid artery using optical vibrocardiography, Med. Eng. Phys. 30 (2008) 490–497.

[6] U. Morbiducci, L. Scalise, M.D. Melis, M. Grigioni, Optical vibrocardiography: a novel tool for the optical monitoring of cardiac activity, Ann. Biomed. Eng. 35 (2006) 45–58.

[7] T.L. Szabo, Diagnostic Ultrasound Imaging: Inside Out, Elsevier, 2014.

[8] L.V. Wang, H.-I. Wu, Biomedical Optics, John Wiley & Sons, Inc, 2009.

[9] L.V. Wang, Photoacoustic Imaging and Spectroscopy vol. 144, CRC Press, 2009.

[10] L.V. Wang, Tutorial on photoacoustic microscopy and computed tomography, IEEE J. Select. Top. Quantum Electron. 14 (2008) 171–179.

[11] C. Tian, T. Feng, C. Wang, S. Liu, Q. Cheng, D.E. Oliver, X. Wang, G. Xu, Non-contact photoacoustic imaging using a commercial heterodyne interferometer, IEEE Sensors J. 16 (23) (2016) 8381–8388.

[12] G. Paltauf, R. Nuster, M. Haltmeier, P. Burgholzer, Experimental evaluation of reconstruction algorithms for limited view photoacoustic tomography with line detectors, Inverse Problems 23 (2007) S81–S94.

[13] X. Zhang, J.R. Fincke, C.M. Wynn, M.R. Johnson, R.W. Haupt, B.W. Anthony, Full noncontact laser ultrasound: first human data, Light, Sci. Appl. 8 (2019) 119.

[14] P. Chiariotti, C. Rembe, P. Castellini, M. Allen, Laser Doppler Vibrometry Measurements in Structural Dynamics, Springer, New York, 2020, pp. 1–45.

[15] C. Rembe, L. Mignanelli, Introduction to Laser-Doppler Vibrometry, Springer International Publishing, 2020, pp. 9–21.

[16] G. Xu, C. Wang, T. Feng, D.E. Oliver, X. Wang, Non-contact photoacoustic tomography with a laser doppler vibrometer, in: A.A. Oraevsky, L.V. Wang (Eds.),

Photons Plus Ultrasound: Imaging and Sensing 2014, vol. 8943 of SPIE Proceedings, 2014, p. 894332. SPIE.

[17] R.W. Haupt, C.M. Wynn, System and Method for Non-contact Ultrasound, 2015.

[18] E. Olsson, P. Gren, M. Sjödahl, Photoacoustic holographic imaging of absorbers embedded in silicone, Appl. Opt. 50 (2011) 2551–2558.

[19] L. Mignanelli, C. Rembe, Feasibility study of the employment of laser doppler vibrometry for photoacoustic imaging, J. Phys. Conf. Ser. 1149 (2018), 012028.

[20] G.J. Diebold, Photoacoustic monopole radiation: waves from objects with symmetry in one, two, and three dimensions, in: L.V. Wang (Ed.), Photoacoustic Imaging and Spectroscopy, CRC Press, 2017, pp. 3–18.

[21] R.O. Esenaliev, A.A. Karabutov, F.K. Tittel, B.D. Fornage, S.L. Thomsen, C. Stelling, A.A. Oraevsky, Laser optoacoustic imaging for breast cancer diagnostics: limit of detection and comparison with x-ray and ultrasound imaging, in: B. Chance, R. R. Alfano (Eds.), Optical Tomography and Spectroscopy of Tissue: Theory, Instrumentation, Model, and Human Studies II, SPIE, 1997, pp. 71–82. SPIE Proceedings.

[22] G.J. Diebold, P.J. Westervelt, The photoacoustic effect generated by a spherical droplet in a fluid, J. Acoust. Soc. Am. 84 (1988) 2245–2251.

[23] A. A. Oraevsky and A. A. Karabutov, "Ultimate sensitivity of time-resolved optoacoustic detection," in Biomedical Optoacoustics, A. A. Oraevsky, ed. (SPIE, 2000), SPIE Proceedings, pp. 228–239.

[24] B. Cox, J.G. Laufer, S.R. Arridge, P.C. Beard, Quantitative spectroscopic photoacoustic imaging: a review, J. Biomed. Opt. 17 (2012), 061202.

[25] X. Zhou, N. Akhlaghi, K.A. Wear, B.S. Garra, T.J. Pfefer, W.C. Vogt, Evaluation of fluence correction algorithms in multispectral photoacoustic imaging, Photoacoustics 19 (2020), 100181.

[26] G. Rousseau, A. Blouin, J.-P. Monchalin, Non-contact photoacoustic tomography and ultrasonography for tissue imaging, Biomed. Opt. Express 3 (2012) 16–25.

[27] A.A. Oraevsky, Optoacoustic tomography of the breast, in: L.V. Wang (Ed.), Photoacoustic Imaging and Spectroscopy, CRC Press, 2017, pp. 411–429.

[28] M. Schewe, D. Kohlmann, H. Wulfmeier, H. Fritze, C. Rembe, Methoden zur Minimierung des Rauscheinflusses durch Hitzeflimmern bei einem heterodynen Laser-Doppler-Vibrometer, tm -Tech. Mess. 87 (2020) 44–49.

[29] I. Daubechies, Ten Lectures on Wavelets (Society for Industrial and Applied Mathematics), 1992.

[30] J. Sun, B. Zhang, Q. Feng, H. He, Y. Ding, Q. Liu, Photoacoustic wavefront shaping with high signal to noise ratio for light focusing through scattering media, Sci. Rep. 9 (2019) 4328.

[31] J.R. Fincke, C.M. Wynn, R. Haupt, X. Zhang, D. Rivera, B. Anthony, Characterization of laser ultrasound source signals in biological tissues for imaging applications, J. Biomed. Opt. 24 (2018) 1–11.

[32] V.E. Gusev, A.A. Karabutov, Laser Optoacoustics, American Inst. of Physics, 1993.

[33] S. Hartmann, R.R. Gilbert, Identifiability of material parameters in solid mechanics, Arch. Appl. Mech. 88 (2018) 3–26.

[34] G.D. Ludwig, The velocity of sound through tissues and the acoustic impedance of tissues, J. Acoust. Soc. Am. 22 (1950) 862–866.

[35] J.G. Koelzer, G. Mitic, J. Otto, W. Zinth, Measurements of the optical properties of breast tissue using time-resolved transillumination, in: S. Avrillier, B. Chance, G. J. Mueller, A.V. Priezzhev, V.V. Tuchin (Eds.), Photon Transport in Highly Scattering Tissue, 1995, pp. 143–152. SPIE. SPIE Proceedings.

[36] Safety of laser products - Part 1: Equipment classification and requirements (IEC 60825–1:2014), Standard, International Electrotechnical Commission, Geneva, CH, 2014.

[37] C. Rembe, M. Wörtge, A. Dräebenstedt, T. Braun, Optical interferometer and vibrometer with such an optical interferometer, 2017 (EP2808644B1, 01.11.2017).